Enhancing airborne LiDAR data for improved forest structure representation in shortwave transmission models

ENHANCING AIRBORNE LIDAR DATA FOR IMPROVED FOREST STRUCTURE REPRESENTATION IN SHORTWAVE TRANSMISSION MODELS

Clare Webster[1,2,3*], Giulia Mazzotti[1,4], Richard Essery[3], Tobias Jonas[1]

[1]WSL Institute for Snow and Avalanche Research SLF, CH-7260 Davos Dorf, Switzerland

[2]Swiss Federal Institute for Forest, Snow and Landscape Research WSL

[3]School of Geosciences, University of Edinburgh, UK

[4]Laboratory of Hydraulics, Hydrology and Glaciology VAW, ETH Zurich, Zurich, Switzerland

Correspondence to: Clare Webster, clare.webster@slf.ch

ABSTRACT

Forest canopies act as intermediaries in radiation energy exchange between the atmosphere and the snow surface. The size, location and distribution of forest discontinuities are important controls on forest shortwave radiation transmission and subsequent snow surface shading and radiation energy exchange between the atmosphere and the canopy, but challenges arise when accounting for these vegetation characteristics at large spatial scales. Airborne LiDAR datasets contain detailed information about canopy structure across large spatial scales which can be exploited within 2D transmission models. However, airborne LiDAR data typically does not resolve lower canopy elements, leading to unrealistic depictions of individual trees. We present a methodology

to enhance airborne LiDAR data by calculating additional trunk and branch points based on segmentation of a canopy height model, allowing more accurate estimates of canopy shortwave transmissivity. To demonstrate this, we deployed a computationally efficient 2D radiation transfer modelling framework that calculates direct and diffuse radiation from a set of distributed synthetic hemispherical images. The model can predict incoming direct and diffuse solar radiation at the snow surface at high spatial (meter-scale) and temporal (minute-scale) resolutions. Comparison between synthetic and real hemispherical photographs showed that synthetic images, if based on enhanced LiDAR data, featured canopy and individual tree crowns that were much denser than the original LiDAR portrays, improving the representation of vegetation structure especially within dense environments and along canopy edges. Corresponding modeled total shortwave radiation matched well with spatially gridded measurements from a moving pyranometer at two sites, where model RMSE was reduced to 59 and 29 W m^{-2} from 181 and 138 W m^{-2}, respectively, compared to the same transmission model with the original LiDAR data. Maps of snow surface shading patterns corresponded well to those seen in aerial photographs, showing the enhanced LiDAR data can be used to solve complex spatiotemporal patterns of sub-canopy incoming radiation. This work demonstrates that canopy structure information from the lower canopy is an important aspect for accurate radiation transfer modelling, and methods presented here can successfully mitigate problems inherent in many airborne LiDAR datasets to improve spatially distributed estimates sub-canopy shortwave radiation.

KEYWORDS

Shortwave radiation modelling

Forest canopy

Airborne LiDAR

LiDAR enhancement

Vegetation shading

Radiative transfer

Ray tracing

Irradiance

Canopy segmentation

Hemispherical photography

Synthetic hemispherical images

1 INTRODUCTION

Complex three-dimensional forest canopies cause spatially and temporally varying solar radiation transmission to the understory, where it is a major component of the sub-canopy surface energy budget (Link and Marks, 1999). Fundamental forest processes such as photosynthesis, snowmelt, moisture availability, evapotranspiration, succession, decomposition, understory growth, and carbon uptake are all influenced by the magnitude and duration of sub-canopy shortwave radiation (Baldocchi et al., 2000; Bales et al., 2011; Breshears et al., 1997; Haddad et al., 2015; Hardy et al., 2004; Harpold et al., 2014; King et al., 2012; Law et al., 2002; Leuschner and Rode, 1999; Wan et al., 1996).

The variable forest structure in relation to the solar position and surrounding topography controls the spatial and temporal variability of the transmission of shortwave radiation, resulting in variable sun-flecks and shadows dominated by direct and diffuse radiation, respectively. These fine-scale variabilities of sub-canopy shortwave radiation influence the reflectivity of the land surface by reducing the overall effective albedo (Ni and Woodcock, 2000; Nolin, 2004; Vikhamar and Solberg, 2002; Webster and Jonas, 2018). For example, above- and below-canopy measurements have demonstrated a correlation between effective forest snow albedo and solar angle, linking a reduction in land surface reflectivity over forest snow surfaces at higher zenith angles with increases in shadow view-fraction over the snow surface (Malle et al., 2019; Nolin, 2004; Webster and Jonas, 2018). Canopy shading has also been shown to affect accuracy of optical remote sensing, leading to errors in snow cover estimates (Kane et al., 2008; Raleigh et al., 2013). Prediction of fine-scale timing and distribution of shadows therefore have important applications within both land surface modelling and satellite observations.

At the point scale, hemispherical photography (HP) is the most common tool used to characterize forest structure and estimate sub-canopy shortwave radiation. HP uses upward-looking images with a 180° (hemispherical) field of view fisheye lens that captures the location of canopy components in view from the point of interest. Hemispherical photographs (HPs) are used to estimate effective leaf area index (LAI) and sky-view fraction (V_f), defined here as the visible portion of sky in the hemispherical view, weighted by the cosine of zenith angle. These canopy variables can then be used within the Beer-Lambert Law to estimate sub-canopy shortwave radiation, which assumes an exponential reduction in solar radiation as it passes through the canopy with horizontal canopy homogeneity (Hardy et al., 2004; Nijssen and Lettenmaier, 1999). The assumption of canopy homogeneity means the law is limited in its application in spatially heterogeneous forests. Beer's Law has been expanded to incorporate calculated solar position (azimuth and zenith angles in polar coordinates) with a directional gap fraction, which has yielded accurate estimates of shortwave radiation in forest gaps (Sicart et al., 2004; Lawler and Link, 2011). In general, however, these methods still include some generalization or homogenization of canopy structure and are less suitable in spatially heterogeneous canopies.

Modelling methods that generalize the canopy structure in the path of the solar beam either in space or time have been demonstrated to be limited in their ability to accurately estimate the brief periods of sun-flecks in the sub-canopy (Musselman et al., 2012a). More accurate directional HP methods use calculated sun position and canopy transmissivity in front of the solar disc calculated from hemispherical images (Jonas et al., 2020; Musselman et al., 2012a; Reid et al., 2014). A solar transmission model developed by Jonas et al. (2020) and applied to high resolution hemispherical photographs produced highly accurate estimates of sub-canopy shortwave radiation. In particular,

97 in at a single point application, their solar transmission model was able to accurately reproduce
98 measured sub-canopy shortwave radiation at the fine temporal scale of individual sun-flecks. It
99 remains impractical, however, to collect the photographs required for spatially distributed
100 modelling. Although it is technically possible to collect thousands of hemispherical images across
101 landscape-scale forested areas, accurately threshold the images and analyze each for V_f and
102 shortwave radiation transmissivity, instead, it may be more efficient to utilize methods that exploit
103 LiDAR (light detection and ranging) data.

104 Methods to calculate synthetic hemispherical images have been developed using terrestrial and
105 airborne LiDAR data through converting the Cartesian coordinates of returns to a spherical
106 coordinate system relative to a point, or virtual "camera" position within the sub-canopy
107 (Alexander et al., 2013; Hancock et al., 2014; Moeser et al., 2014; Varhola et al., 2012). This
108 method for obtaining canopy structure information has the advantage of generating spatial maps
109 of hemispherical photograph-derived metrics such as gap fractions, canopy closure, V_f or LAI.
110 While terrestrial laser scanning (TLS) produces highly accurate synthetic images (Hancock et al.,
111 2014), data collection is relatively time intensive and it is limited in spatial scope for radiation
112 modeling at spatial domains beyond 100m. Airborne acquisition of LiDAR data increases the
113 spatial scope of data available for modelling, but is currently limited by data resolution.

114 While TLS datasets can have point densities in the range of > 1000 points m^{-2}, airborne LiDAR
115 datasets are considered high resolution with point densities closer to 10 points m^{-2}. These lower
116 point densities mean specific structural elements in the canopy, i.e. trunks and individual branches,
117 are not well represented when creating synthetic images (e.g. Varhola et al., 2012), which results
118 in the overestimation of V_f and inaccurate timing and magnitude of modelled sub-canopy

shortwave radiation. A solution to this has been to rely on a point-size calibration using real hemispherical photographs and calculated V_f in order to increase the projection of each LiDAR point in the synthetic images, where larger projected point sizes compensate low LiDAR point density. These large point sizes have resulted in relatively accurate estimates of V_f and other forest descriptor variables (Moeser et al., 2014; Zellweger et al., 2019a). However, there is a trade-off between increases in point size and a loss in realistic representation of the canopy structure. Resulting images fail to accurately represent individual canopy structural elements and particularly those elements that reside in the lower canopy if LiDAR was acquired from above. While reasonably accurate predictions of diffuse radiation can be determined using the V_f estimates, modelling sun-flecks at high temporal resolutions is severely hampered with hemispherical images generated using the point-size calibration method.

Several studies have used synthetic images within traditional HP analysis software such as Hemisfer (Moeser et al., 2014; Schleppi et al., 2007) or Gap Light Analyzer (Frazer et al., 1999; Varhola et al., 2012) to arrive at an estimate of hourly or daily shortwave radiation. Another method to model shortwave radiation using LiDAR has been developed from the relationship between the penetration of a LiDAR beam through the canopy and a direct beam of shortwave radiation. As a result, LiDAR data has been used to estimate biophysical parameters such as LAI or canopy cover and light transmittance (Barilotti et al., 2006; Bode et al., 2014; Essery et al., 2008; Morsdorf et al., 2006; Nyman et al., 2017), which can be used within a Beer's-type model. The use of spatial maps of LAI, however, maintains the same limitations of the Beer's-type model, while use of individual synthetic hemispherical images is restricted by the limited representation of the individual canopy structure elements. Either of these methods would result in significant

errors when modelling across large areas of heterogeneous forests. Highly spatially and temporally accurate estimates of canopy structure and sub-canopy shortwave radiation at larger spatial scales therefore require a more accurate representation of individual canopy elements and their consideration in relation to the solar path.

Methods applied at watershed scales (> 500 m x 500 m) that utilize airborne LiDAR data include three-dimensional ray-tracing methods (e.g. Musselman et al., 2013; Tymen et al., 2017) or GIS-based solar radiation models (e.g. Bode et al., 2014). These models account for the directionality of the solar path relative to the canopy structure, but either ignore or poorly estimate diffuse radiation when compared to measured values (Bode et al., 2014). Other radiative transfer models have been demonstrated to produce realistic estimates of sub-canopy solar radiation across the shortwave radiation spectra (Widlowski et al., 2015), but at smaller spatial scales than models by Musselman et al., (2013) or Bode et al. (2014). An ongoing limitation of these types of models is their computational efficiency, affecting the spatiotemporal extent and/or resolution of the calculations and the detail of canopy structure accounted for. For example, these limitations have meant that model output is often restricted to snapshots during the solar year (e.g. Musselman et al., 2013), and temporally continuous modelling throughout seasonal or annual cycles is impractical. This hinders the use of model output within land surface models, which could benefit from detailed canopy transmittance information. Furthermore, few of these models have been tested against distributed radiometer measurements of real sub-canopy shortwave radiation (Bode et al. 2014).

The calculation of high-resolution canopy transmissivity along the solar track in a synthetic hemispherical image has so far been limited by the resolution and lack of forest structural detail of

airborne LiDAR datasets. Recent advances in forest LiDAR analysis have led to development of freely available algorithms that can easily identify individual tree crowns and locations of canopy maxima in high resolution canopy height models (Hamraz et al., 2017; Plowright, 2018). These tools facilitate automatic identification of tree trunk and crown locations, and some also include allometric equations for calculation of forest structural parameters (Dalponte and Coomes, 2016). These tools are yet to be used within the context of enhancing LiDAR data point densities, or within the context of modelling sub-canopy shortwave radiation.

This work presents a LiDAR enhancement methodology that utilizes new forest segmentation tools in order to add trunk and branch points to better represent crown densities and lower canopy elements. The enhanced LiDAR is then used to calculate synthetic hemispherical images with realistic representation of individual canopy structural elements. Realistic synthetic hemispherical images are then combined with the solar radiation algorithm from Jonas et al. (2020) for modelling sub-canopy direct and diffuse shortwave radiation in a sub-alpine coniferous forest. Optimization and parallelization of LiDAR enhancement, synthetic image generation and shortwave radiation calculations increase computational efficiency and enable application of this method at high spatial and temporal resolution over large surface areas, allowing for spatially and temporally contiguous model output. In this study the model is applied at 3×10^5 points at 1 m spatial and 2-minute temporal resolution for an entire annual solar cycle. The method is calibrated using real hemispherical photographs and validated using spatially distributed measurements of sub-canopy total shortwave radiation and high-resolution aerial photographs of snow surface shading. The final output of the methodology is a spatially and temporally continuous maps of diffuse, direct

and total sub-canopy shortwave radiation and shadow distribution at high spatial and temporal resolution.

2 DATA AND MODEL SETUP

2.1 Model Domain

Shortwave radiation modelling was carried out within a 250m x 1200m domain in the eastern Swiss Alps (Figure 1). The forest in the domain is discontinuous in structure and predominantly mature Norway Spruce with some Larch trees. The area was chosen due to its size, discontinuous forest structure for greatest spatial variability in shortwave radiation, minimal buildings and man-made infrastructure within the domain, as well as the availability of validation data from airborne imagery and ground-based radiometers. Mean LiDAR-derived tree height is 28 m, and maximum is 44 m. Surface slopes were less than 5° with the exception of the south-east corner (Figure 1e).

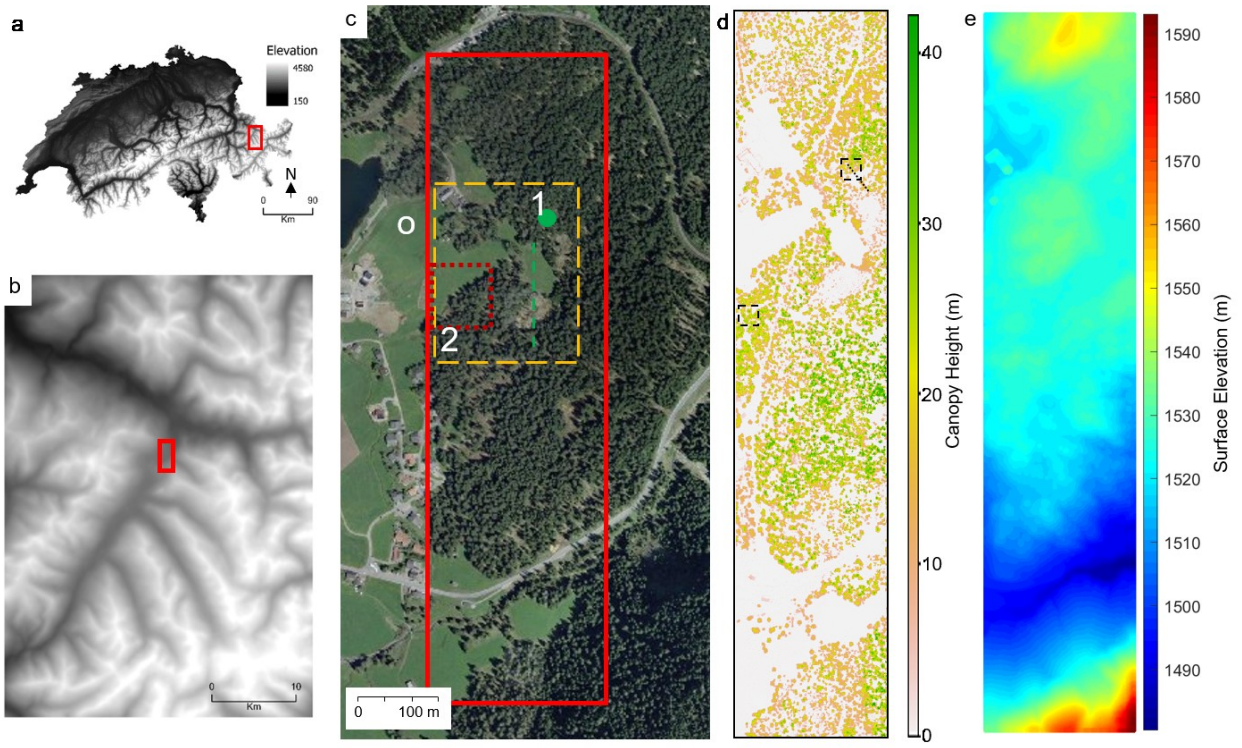

196

197 Figure 1: a) Location of study area within Eastern Swiss Alps and b) surrounding local topography; c) Solid
198 red box outlines larger modelling domain, orange dashed line indicates flight area for aerial photography,
199 dashed red box outlines smaller modelling domain shown in Figures 7 and 11, numbers show radiation
200 measurement grid locations and 'o' shows location of open site; green circle indicates cable car location;
201 green dashed line indicates transect location in Animation 1 in the supplementary material; d) canopy height
202 model of modelling domain with boxed outlines of sites 1 and 2 and cable car location (lines); e) surface
203 terrain height of modelling domain. Aerial imagery downloaded from https://s.geo.admin.ch/842c6f920c.
204 Elevation data in a-b from https://shop.swisstopo.admin.ch/en/products/height_models/dhm25.

205

206 **2.2 Model Input Data**

207 *2.2.1 Airborne LiDAR Data*

208 The surface LiDAR data used in this study was first described in Moeser et al. (2014). Data was
209 acquired in September 2010 using a Riegl LMS Q560 sensor from a series of helicopter flights at

an altitude of 700 m above ground. Wavelength was 1550 nm with pulse durations of 5 ns and up to 7 returns per pulse, with a maximum scan angle of ±15°. The LiDAR covering the modelling area in this study has a point density of 42 points m^{-2} for all returns.

2.2.2 Terrain Data

Solar radiation models are highly scale dependent, particularly in topographically complex regions. Both distant and local topography have a strong influence on the radiation reaching the top of the canopy as well as the ground where uneven terrain at meter scales blocks radiation at low solar angles. Ray tracing and other transmission models either ignore distant and local terrain shading or require a large model domain that also includes distant shading topography when operating in mountainous regions. Within dense forests, incoming solar radiation can usually be sufficiently represented by accounting for only surface and local terrain data, as the influence of distant topography is less significant. In sparse and discontinuous forests in complex topographical environments, distant and local topography must both be included in order to block the solar radiation particularly in the beginning and at the end of the day (Zellweger et al., 2019a).

A digital terrain model (DTM), used to characterize the local terrain (e.g. minor surface slopes), was created by classifying the ground points in the airborne LiDAR data using LAStools (https://rapidlasso.com/lastools/). Using only the ground points, a triangulation-based interpolation was applied to the dataset in order to fill any gaps, which were particularly present below denser forest canopy. The resulting surface was then resampled and gridded at 1 m resolution. This local DTM was also used to estimate the height of the LiDAR data points above the terrain surface. A coarser, regional, DTM with a 50m resolution derived from the Swiss

national topographical map was used to represent the distant topography within the synthetic images (source: https://shop.swisstopo.admin.ch/en/products/height_models).

2.2.3 Above-canopy shortwave radiation data

Shortwave radiation measured at a local open, un-forested site in the center of the model domain (Figure 1) was used to represent above-canopy conditions. For this purpose, a Kipp and Zonen CMP3 broadband pyranometer (300-2800 nm), recording incoming shortwave radiation at 1-second intervals, was installed on a tripod with a ball head for accurate levelling. Data from this pyranometer was used for modelling sub-canopy radiation for comparison with measured data (Table 1).

Table 1: Summary of canopy structure and data acquisition times for forest and open sites. Details of acquisition of hemispherical photographs (HPs) are classified as either validation (v) or calibration (c) measurements. Measurements were taken from a cable car (c.f. 2.3) and using a motorized gimbal set up (c.f. 2.4) and at an open site.

		V_f range	HPs	Pyranometer measurements
Gimbal	Site 1	0.03-0.44	29.03.2019 (v)	28.03.2019 12:00
	Site 2	0.04-0.22	28.03.2019 (v)	28.03.2019 11:00
Open Site				28.03.2019
Cable Car		0.11-0.50	06.03.2019 (c)	-

2.3 Calibration Data

Real HPs were taken using a Sony Alpha NEX6 16.1MP camera with a Yasuhara Madoka f/4 7.3 mm 180° fisheye lens. Photographs were taken on a cable car at 2 m above ground height along a 60 m transect in the center of the model domain in March 2019 (Figure 1c-d). In total, 42 images were selected for the calibration procedure. Sky-view fraction across the transect varied between 0.1 and 0.5.

2.4 Validation Data

2.4.1 Canopy structure

Real HPs were taken along gridded transects at 1.5 m height using a motorized gimbal set-up, developed for nonstationary continuous measurements of canopy structure and sub-canopy radiative regimes (Mazzotti et al., 2019). Two sites (Figure 1c-d) consisted of eight transects of 40 m length, arranged to form a grid of four parallel lines perpendicular to the other four. Photographs were taken at approximately 2-m intervals along each of the 8 transects per site, using a Canon EOS 600D SLR camera with a sigma 4.5mm EX DC fisheye lens. All photographs were taken in March 2019 (Table 1).

All HPs from both camera set-ups were taken during either high solar zenith angles or overcast sky conditions to inhibit direct insolation in the frame, which would hamper image analysis. Photographs were thresholded using the adaptive thresholding algorithm from Jonas et al. (2020). This algorithm tracks local sky brightness across the frame, which is particularly important when

images are taken during high solar zenith angles and clear sky conditions. Sky-view fraction for each photograph was calculated using the HPEval software from Jonas et al. (2020), which is available under https://github.com/Tobias-Jonas-SLF/HPEval.

2.4.2 Sub-canopy shortwave radiation measurements

Sub-canopy shortwave radiation measurements were collected at two forest sites (Figure 1c-d) along the gridded transects following the methods developed in Mazzotti et al. (2019). The same motorized gimbal set-up as used for the acquisition of HPs was fitted with the same Kipp and Zonen CMP3 pyranometer as the open site and carried along the transects at a constant slow walking pace of approximately 0.15 ms^{-1}. Data were recorded at 1-second intervals and time stamps were recorded at each intersection point. A summary of the data collection is shown in Table 1, and further details on data post-processing can be found in Mazzotti et al. (2019).

2.4.3 Aerial Imagery

An airborne imaging survey was carried out across a 300 m x 360 m in the central area of the model domain (Figure 1c) during clear-sky conditions and full ground snow cover. The survey involved three separate flights during morning, midday and afternoon on 28 March 2019. Flights were carried out with a DJI Phantom UAV flying at 100 m above ground level. Images were stitched into an orthomosaic using Agisoft Photoscan Pro.

3 MODELLING METHODOLOGY

3.1 LiDAR enhancement

The methodology described in this section was written as a series of R and MATLAB® scripts to run on a normal laptop computer with 16GB RAM.

The canopy segmentation methodology is demonstrated in Figure 2 over a 200 m x 200 m region in the center of the model domain. A pit-free canopy height model (CHM) with 0.5 m resolution was calculated over the model domain using LAStools and the methods described in Khosravipour et al., (2014), who demonstrated that this method significantly improved the accuracy of tree detection (Figure 2a). Points within the model domain classified as buildings using LAStools classification methods were removed for CHM generation and canopy segmentation calculations in order to avoid roof tops being erroneously identified as canopy maxima.

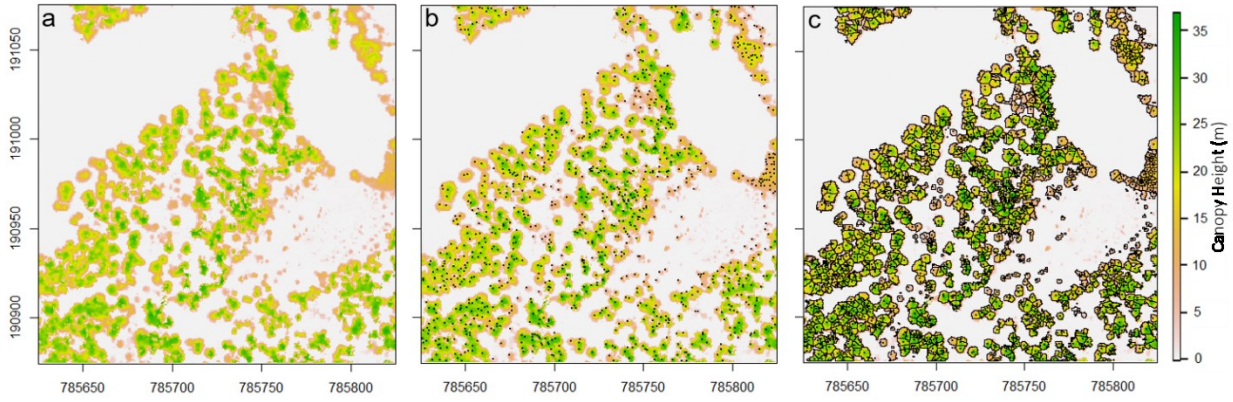

Figure 2: Canopy height model at 0.5 m resolution (a), with location of canopy maxima (b) and individual canopy segments (c) for an example 200 m x 200 m area in center of the model domain.

Individual tree crowns were identified using the R package *rLiDAR* (Silva et al., 2017), through a search algorithm that identified the location of local canopy maxima in the CHM (Figure 2b). The

CHM was then segmented using a tree crown segmentation algorithm within the same R package, which delineates and computes ground projected area of individual tree crowns. Although many tree crown delineation algorithms exist, *rLiDAR* was selected as it works on the canopy height model, rather than the raw LiDAR. This resulted in denser tree crown maps particularly in the denser areas of the canopy where individual tree crowns share boundaries (Figure 2c), whereas other algorithms that worked on the raw LiDAR left gaps between overlapping tree crowns. The method of choice here meant a higher number of individual points within the original LiDAR could be associated with individual tree crowns, leading to denser branch networks.

Additional LiDAR points were added below the location of the canopy maxima in each tree crown to represent opaque trunks. Use of this method relied of two assumptions. The first was that the LiDAR accurately measured the top of each tree crown. While this was unlikely, due to the density of the LiDAR dataset used here, we assume the canopy maxima were identified within the 0.5 m resolution of the canopy height model. The second assumption was that tree trunks were completely vertical. This assumption is suitable for Norway spruce, but alternatives would need to be developed for species that do not have a central and near vertical stem.

With the height and crown diameters of each individual tree identified, diameter of the trunk at breast height was calculated within the R package *itcSegment* (Dalponte, 2016) following the allometric equations of Jucker et al. (2017). These equations were derived from a global database of > 100,000 trees for which stem diameter, height and crown diameter have been measured, with specific algorithms for individual biomes. In this study, biome '19' (Palearctic-Temperate coniferous forests-Gymnosperm) was selected.

Stem diameter at breast height, height and location of each individually identified tree were used to generate points representing tree trunks in the enhanced LiDAR. Cylinders were used between the ground up to breast height (1.5 m), and a linear conical shape was then used from 1.5 m up to the individual tree height to represent the natural taper of tree trunks (Gray, 1956). All trunks were generated with the same point density that ensured they were represented as opaque in the resulting synthetic hemispherical images.

Branches were added to the LiDAR by first classifying the original LiDAR points by the tree crown in which they were located (points located outside of segment boundaries were left unclassified). Each tree crown segment was assigned a random branch angle between 60 and 100° (0° being vertical growing upwards and 90° being horizontal), based on ranges presented in Colin and Houllier, (1992) and Mäkinen and Hein, (2006) for Norway spruce trees. New branch points were then created between each point in the original LiDAR data and the associated tree trunk along the randomly assigned branch angle axis at 0.15 m intervals. Spacing between the additional branch points provided a more realistic representation of tree crown density compared to a continuous line, allowing some light to penetrate through the canopy (see Animation 1, supplementary material).

The dataset with additional trunk and branch points is hereafter referred to as the enhanced LiDAR, while the dataset without additional points is referred to as the original LiDAR.

3.2 Generating synthetic hemispherical images

The generation of a synthetic hemispherical image at a point required the LiDAR surface data and the DTMs at high and coarser resolutions, following the methods developed in Moeser et al. (2014) and extended by Zellweger et al. (2019a), who added the terrain shading feature. The following procedure was written in MATLAB® and calculations were carried out using the MATLAB parallel computing toolbox on a 64 core Linux Server.

3.2.1 Creation of synthetic image matrix

The angular perspective of real HPs was replicated by converting the Cartesian coordinates of the original or enhanced LiDAR points to a spherical coordinate system based on the point of origin (i.e. Cartesian XYZ coordinates of the virtual "camera" location). Previous methods used LiDAR coordinates to populate a spherical-coordinate scatter plot (e.g. Varhola et al., 2012; Moeser et al., 2014), however this method is less suitable for modelling at the larger spatial scales presented here due to computational constraints of generating and saving large numbers of image files. Operation of these plotting methods on Linux servers or high-performance cluster computers require graphics support, which is often not available. Instead, we created an empty "sky-view" matrix comprised of sky coordinates that is subsequently occupied by the LiDAR data points and calculated terrain masks.

An image radius (r) of 500 pixels was chosen as a trade-off between computational efficiency and spatial resolution of canopy representation in the images. The empty matrix was created as an XY mesh grid from 0 to $2r$, with dimensions of $2r$ x $2r$. Radial distance from the center of the grid was calculated, and all points at distances larger than r (i.e. below local horizon) were removed. The

362 coordinates of the empty image matrix were converted to a relative system, where (0,0) is the
363 center of the image matrix and X_{max} and Y_{max} represent the outer ring of the synthetic hemispherical
364 grid space. All synthetic hemispherical images were calculated with an equiangular lens
365 projection.

366 *3.2.2 Canopy and terrain representation*

367 Cartesian coordinates of the LiDAR and enhanced data points were converted from the absolute
368 to a relative coordinate system based on the point of origin. At this stage, data outside the user-
369 defined buffer zone were removed from further analysis in order to save computational time. This
370 buffer zone was 100 m for the LiDAR data, 50 m for the trunks, and 30 m for the branch points.
371 A narrower buffer was selected for the trunk and branch points as the original LiDAR data was
372 dense enough to accurately represent distant canopy elements in the synthetic images without the
373 need for the additional points. Data points were then converted to the spherical system, where the
374 output is an azimuth and zenith angle and a radial distance from point of origin. Azimuth is the
375 angle in the x/y plane measured in radians from the positive x axis, zenith is the angle from the
376 vertical and radial distance is the Euclidean distance between the surface points and the point of
377 origin.

378 Using the spherical coordinate system, points that were not visible from the virtual "camera"
379 perspective due to occlusion by closer points were removed from the dataset. At locations where
380 trunks were located within 5 m of the virtual "camera" position, the original density of trunk points
381 resulted in semi-transparent trunks in the synthetic images. In such cases the density of the tree
382 trunk points was increased. This location-based iterative method was substantially more

383 computationally efficient than simply prescribing a larger point density for all tree trunks in the
384 model domain.

385 Local and distant terrain masks in the synthetic images were each calculated from the two DTMs.
386 After conversion to the relative coordinate system, the topographic horizon line was calculated by
387 determining the maximum zenith angle of all terrain points within each 1° azimuth increment and
388 within the 300 m and 10 km topographic radii of the two DTMs (local and coarse, respectively)
389 following Zellweger et al. (2019a). A dense matrix of points was created below these horizon lines
390 to ensure these regions were 100% opaque in the final synthetic images.

391 The azimuth and zenith points of the canopy data and terrain matrices were converted to the 2-
392 dimensional Cartesian XY coordinates of the sky-view matrix, where (0,0) represents a point
393 located directly above the point of origin. The empty sky-view matrix was occupied by the canopy
394 and terrain points through a classification procedure that determined which coordinates of the
395 empty matrix overlapped with the coordinates of the canopy and terrain points within a threshold
396 distance. This threshold distance determined the projected size of each LiDAR data point within
397 the final synthetic hemispherical image, whereby a larger threshold distance resulted in a larger
398 projected point size, and vice versa. A projected point size distribution within the images was
399 created by linearly decreasing the threshold distance with increasing radial distance from the point
400 of origin as suggested by results in Moeser et al. (2014). The calibration procedure to determine
401 the optimal point size distribution is briefly described in the following section. The result of this
402 image classification procedure is a binary matrix which has the same structure as a binarized
403 hemispherical photograph.

3.2.3 Calibration of projected point size

Forty-two HPs taken along a transect ("Cable Car" in Table 1) were used to calibrate the projected point size distribution within the synthetic images. The ratio of black to white pixels in each 10° zenith ring of the real images was calculated using the HPEval software, which accounts for non-equiangular lens projection in the real photographs. At each location corresponding to a real hemispherical photograph, seventeen synthetic images were generated with a range of point sizes, resulting in 714 synthetic images for comparison. The optimal projected point size distribution was selected through assessment of calculated root-mean-square error (RMSE) of pixel ratio for each zenith angle ring in each synthetic image as well as visual inspection of representation of individual canopy elements compared to the real photographs.

Two different point size distributions were calibrated from the same photographs. The first was calculated for the enhanced LiDAR dataset. A second distribution, with larger projected point sizes, was determined for the unenhanced, original LiDAR, in line with methods from previous studies such as Moeser et al., (2014) who increased their projected point sizes in order to more accurately estimate canopy closure compared to real HPs.

3.3 Shortwave radiation modelling

Shortwave radiation modelling in this study used the same methods as those developed by Jonas et al. (2020) for high temporal resolution modelling of sub-canopy incoming shortwave radiation using real hemispherical photographs. In their study, RMSE of measured and modelled sub-canopy shortwave radiation data at 1-hour and 10-minute resolutions amounted to 17 and 28 W m^{-2},

425 respectively, which was within the measurement uncertainty of the radiometer used. In this study,
426 we employ the same shortwave transmission model and apply it to the synthetic hemispherical
427 images. A summary of relevant details is provided here. A more detailed description of the model
428 is available in Jonas et al. (2020).

429 *3.3.1 Canopy transmissivity*

430 Sky-view fraction of the synthetic images and real photographs was calculated following Essery
431 et al. (2008), in case of the real HPs accounting for measured non-equiangular lens projection of
432 the two cameras. V_f was calculated from the ratio between the numbers of canopy and sky pixels
433 in each concentric zenith ring, weighted by the cosine of the solar zenith angle. Principally, un-
434 weighted V_f, also known as gap fraction, can also be calculated from these synthetic images.

435 While V_f and diffuse transmissivity are constant in time, the direct-beam transmissivity varies as
436 a function of canopy structure in the path of the direct solar beam, which can be calculated directly
437 from hemispherical images at high temporal resolution. This time-varying canopy transmissivity
438 was determined by the spatial layout of the canopy relative to a straight line between the calculated
439 solar position and the virtual "camera" position. First, local solar position was calculated using the
440 parametrization developed by NOAA
441 (https://www.esrl.noaa.gov/gmd/grad/solcalc/calcdetails.html), resulting in a local azimuth and
442 zenith angle for each location and time step. Within each image, the sun has an apparent diameter
443 of 0.53 degrees, so calculation of solar position and canopy transmissivity at 2-minute intervals
444 yielded a spatially and temporally continuous solar track. For each 2-minute time step, the
445 percentage of pixels classified as sky or canopy in front of the solar disc determined the direct
446 beam canopy transmissivity.

3.3.2 *Sub-canopy shortwave radiation*

Sub-canopy shortwave radiation (SW_{for}) to a horizontal surface was calculated following the formulation in Jonas et al. (2020) by multiplying the canopy direct (τ_{dir}) and diffuse (V_f) shortwave transmissivity by the above-canopy components:

$$SW_{for} = SW_{dif} \cdot V_f + SW_{dir} \cdot \tau_{dir} \quad (1)$$

The above canopy total incoming shortwave radiation (SW_{total}) was divided into SW_{dir} and SW_{dif} through the partitioning schemes from Erbs et al. (1982):

$$\frac{SW_{dif}}{SW_{total}} = \begin{cases} 1 - 0.09\tau_{atm} & \text{for } \tau_{atm} \leq 0.22 \\ 0.95 - 0.16\tau_{atm} + 4.39\tau_{atm}^2 - 16.64\tau_{atm}^3 + 12.34\tau_{atm}^4 & \text{for } 0.22 < \tau_{atm} \leq 0.8 \\ 0.165 & \text{for } 0.8 < \tau_{atm} \end{cases} \quad (2)$$

which describes the fraction of diffuse radiation in terms of the atmospheric transmissivity:

$$\tau_{atm} = \frac{SW_{total}}{I_0 . cos(\theta)} \quad (3)$$

where θ is the solar zenith angle, and I_o = 1367 W m^{-2} is the solar constant.

Above-canopy shortwave radiation was either that measured at the open site (Section 2.2.3) or a modelled maximum potential value. Maximum potential incoming solar radiation was calculated by weighting the solar constant by the cosine of the solar zenith angle. In this case, the atmospheric transmissivity is assumed as 1, thereby calculating the maximum possible radiation reaching the top of the canopy and subsequently transmitted to ground level.

460

461 ### 3.4 Model implementation

462 Synthetic hemispherical images were calculated within the forest sites at the locations of real
463 hemispherical photographs and radiation measurements ("Gimbal" in Table 1). At these sites,
464 images were created using both the enhanced and original LiDAR. Sub-canopy shortwave
465 radiation was calculated at all locations for the measurement periods in Table 1 using measured
466 above-canopy shortwave radiation from the open site as model input. Total shortwave radiation
467 was calculated at 2-minute intervals for all synthetic images.

468 Synthetic hemispherical images at 3×10^5 locations within the model domain were generated using
469 the enhanced LiDAR at 1 m spacing and 0.5 m above local DTM-derived surface elevation.
470 Maximum potential above-canopy shortwave radiation was calculated between 21 December and
471 22 June. In addition, synthetic hemispherical images using the original LiDAR were calculated
472 within the 110 m x 130 m region in the center of the model domain (Figure 1c) for a comparison
473 of the two methods.

474

475 ### 3.5 Model validation

476 Measurements of canopy structure and shortwave radiation at the two forest sites ("Gimbal" in
477 Table 1) were compared with modelled values in order to demonstrate the ability of the model to
478 capture measured spatial distribution at these sites. Thirteen measurement locations within each
479 site were used for statistical evaluation of V_f and eight intersection locations were selected for

480 shortwave radiation. These locations were selected as the accuracy of the position of the
481 measurements could be estimated to < 0.5 m. Additionally the eight shortwave radiation validation
482 locations were located at transect intersection points where the radiometer was stationary for 20
483 seconds to allow the measurements to stabilize. A RMSE, mean bias and mean absolute error
484 (MAE) of V_f and SW_{for} were calculated at all validation locations.

485

486 # 4 RESULTS AND DISCUSSION

487 ## 4.1 Improvements in canopy representation

488 The addition of branch points increased the LiDAR point density from 42 points m^{-2} to 226 points
489 m^{-2}. Further addition of points for creating opaque trunks increased the LiDAR data to a density
490 >1000 points m^{-2}. A 100 m transect through the forest, beginning and ending 20m before and after
491 the cable car transect (Figure 1c), demonstrates the improved representation of the forest structure
492 through the addition of trunk and branch points (Figure 3). With the addition of the calculated
493 trunk and branch points the canopy was noticeably denser in the new synthetic images (Figure 4d-
494 f) compared to the original LiDAR data (Figure 4g-i). The three examples shown in Figure 4 are
495 either close to the canopy edge, or within dense canopy. A further comparison at 381 locations
496 along a transect through the gap in the flight area is shown in Animation 1 of supplementary
497 material. Figure 4 and Animation 1 show lower canopy elements appear much better represented
498 by the enhanced LiDAR. This improvement is particularly important within denser forests, where
499 occlusion by the upper canopy is higher (e.g. Figure 4b, e and h), and close to edges where a

500 combination of thin canopy and limited LiDAR points would lead to overestimated V_f and solar
501 transmissivity (e.g. Figure 4c, f and i).

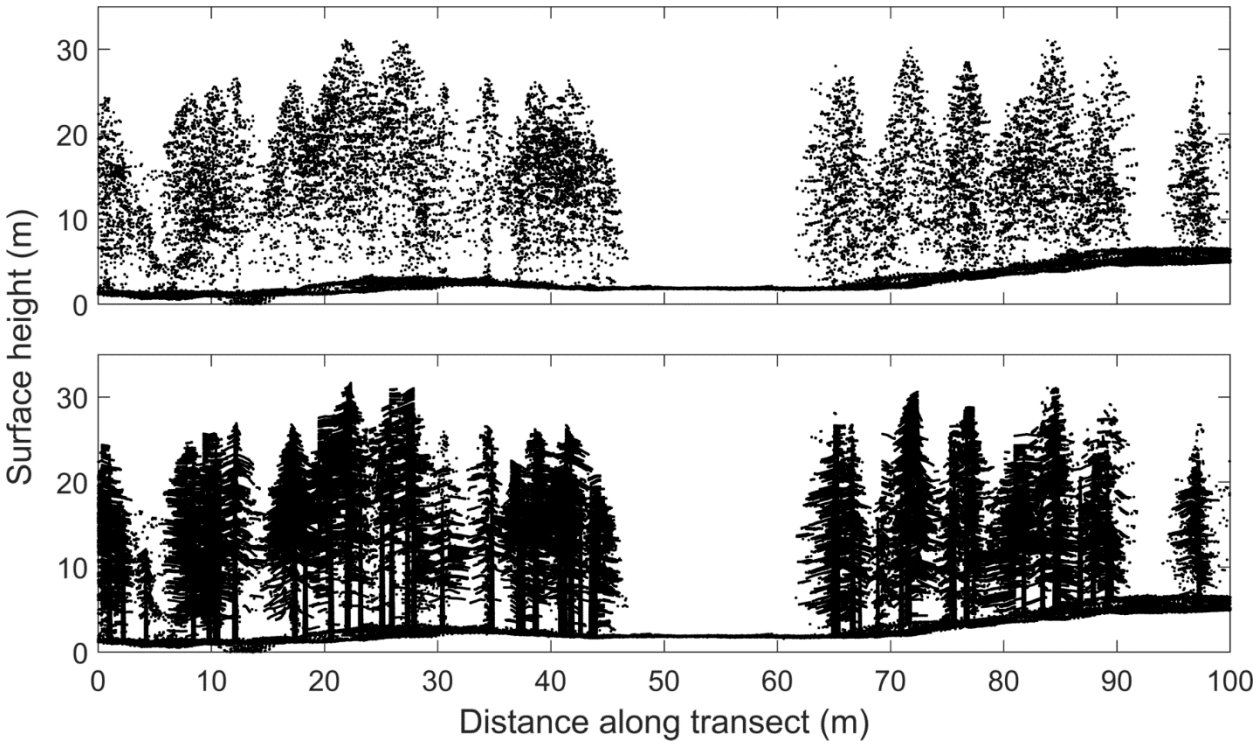

502

503 Figure 3: 15 m wide forest cross section along cable car transect (Figure 1c-d) with original LiDAR (top)
504 and enhanced LiDAR (bottom).

505

506

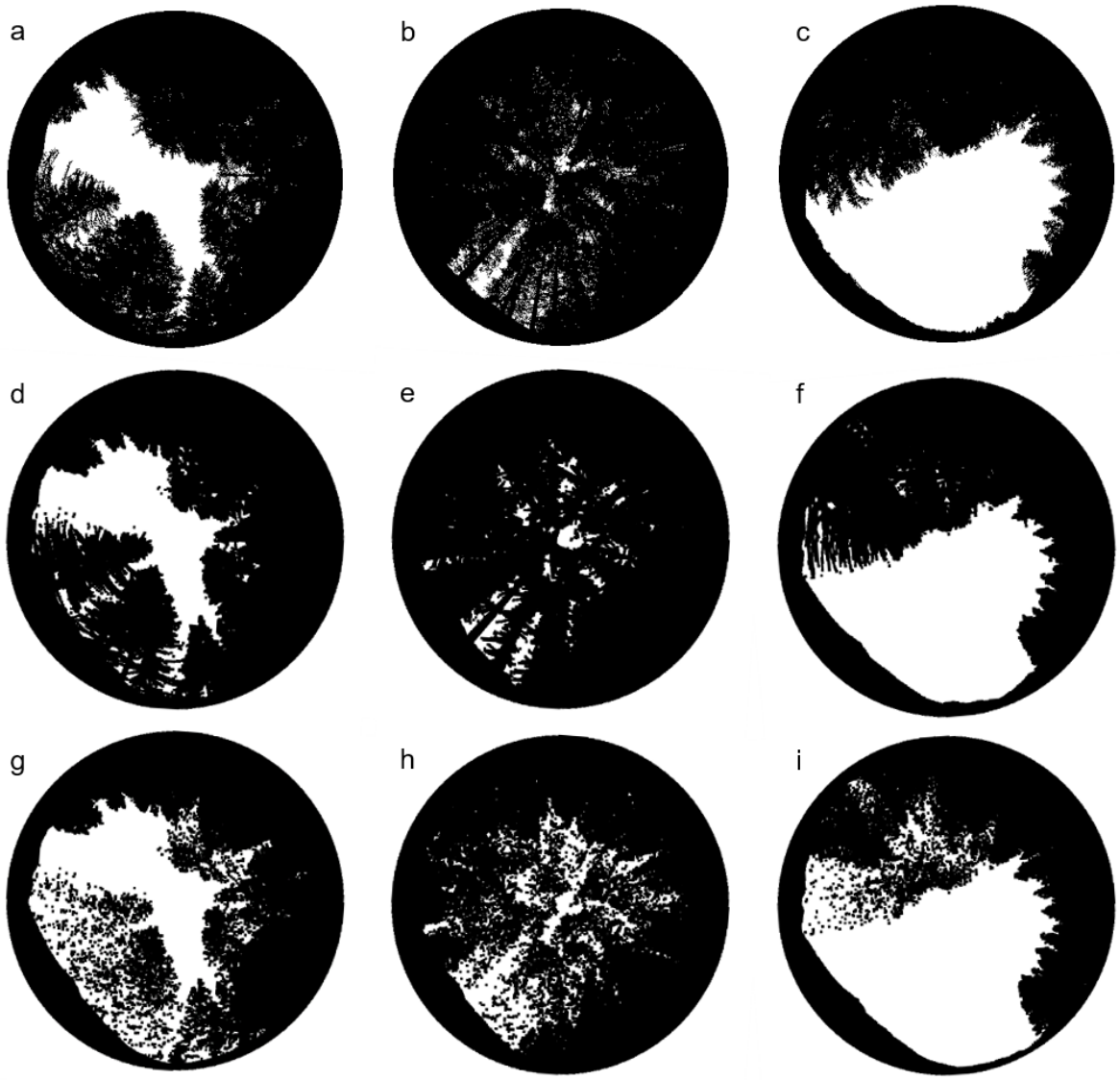

507

508 Figure 4: Real hemispherical photographs (a-c), synthetic hemispherical images from enhanced LiDAR (d-
509 f) and from original LiDAR (g-i) at three sample locations within Figure 2. South at top of picture. Real
510 hemispherical photographs in a-c are radially distorted due to the non-linear projection of the lens
511 (distortion was accounted for in all calculations).

512

513 The lower canopy was largely under-represented in the original LiDAR at all three locations shown
514 in Figure 4. Omissions in the synthetic images in Figure 4g-i are a result of the lower point density
515 of the original LiDAR data, increasing the V_f at each location compared to the real images (Figure

516 4a-c). Importantly, these gaps in the image do not represent real gaps in the forest, thus modelled
517 direct solar radiation transmission through these gaps will not represent real sun-flecks on the
518 ground and total incoming shortwave radiation will be overestimated throughout the year.

519 Calculation of the synthetic images in Figure 4d-f (original LiDAR) and Figure 4g-i (enhanced
520 LiDAR) used different projected point sizes, each calibrated using the same real HPs. While this
521 method can be useful for statistically determining the best point size distribution, unrealistic
522 representation of canopy density the original LiDAR images compared to the real HPs demonstrate
523 that this calibration does not always lead to feasible hemispherical images. This is particularly
524 evident in Figures 4g and h, which were located along edges where there were a limited number
525 of LiDAR points to appropriately represent the lower canopy. Further increasing the projected
526 point size in images at these locations would lead to relatively accurate estimates of diffuse solar
527 radiation (e.g. Varhola et al., 2012). However, this point size increase would 1) decrease the direct-
528 beam transmissivity in other regions of the image; and 2) maintain unfeasibly high direct-beam
529 estimates in regions of the image where the number of LiDAR points is low relative to the canopy
530 density. Ultimately, artificially increasing the point size distribution to better match V_f values and
531 diffuse radiation would reduce the accuracy of the direct-beam component in the shortwave
532 radiation model. Additionally, a larger point size distribution would further increase canopy height
533 and subsequent shadow length in the output canopy shading maps.

534 Results of the calibration procedure at 42 locations along the cable car transect revealed no single
535 projected point size distribution performed best at all locations. Across a wide range of projected
536 point sizes that visibly altered V_f and canopy representation in the synthetic images, the differences
537 of V_f RMSEs between the real photographs and synthetic images were, in general, less than 0.1.

In the absence of real HPs, it would therefore be possible to perform a manual and subjective calibration procedure to check accuracy of the method on different LiDAR datasets.

4.2 Comparison of LiDAR-derived canopy structure variables

Sky-view fraction distributions calculated both from real HPs and synthetic images were relatively similar along all transects at both forest sites (Figure 5). RMSE, mean bias and MAE values show synthetic images from the original LiDAR slightly overestimate V_f compared to those from the enhanced LiDAR (Table 2). The improvement with the addition of trunk and branch points to enhance the LiDAR was particularly noticeable in the denser site (site 2), where the maximum measured V_f was 0.22. In general, at site 2 there was a positive bias in V_f with the original LiDAR compared to the enhanced (Table 2), demonstrating the poorer performance of the original LiDAR in dense forests. Overall, however, statistical error in V_f was low for both LiDAR datasets given both outputs were calibrated for V_f using real hemispherical photographs.

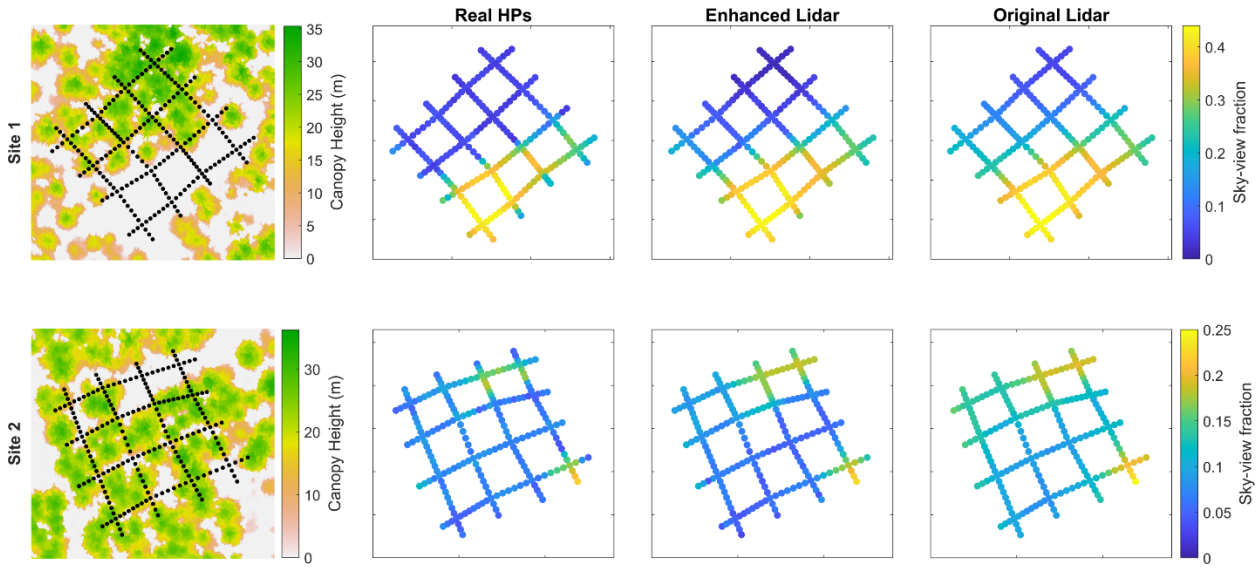

552

553 Figure 5: Canopy height model and estimated V_f from real hemispherical photographs and synthetic
554 hemispherical images from enhanced and original LiDAR at both forest sites. All images are oriented north
555 to the top.

556

557 Table 2: Root mean square error (RMSE), mean bias and mean absolute error (MAE) for sky-view fraction
558 (V_f, dimensionless) and measured shortwave radiation (SWR, W m^{-2}) at the two forest sites.

		Vf		SWR (W m^{-2})	
		Site 1	Site 2	Site 1	Site 2
RMSE	Enhanced	0.02	0.02	59.3	28.7
	Original	0.04	0.04	180.8	137.8
Mean bias	Enhanced	0.01	0.00	-49.0	-0.2
	Original	0.03	0.04	57.5	79.1
MAE	Enhanced	0.02	0.02	49.0	18.1
	Original	0.03	0.04	100.1	88.0

559

4.3 Distributed estimates of sub-canopy shortwave radiation

4.3.1 Comparison to sub-canopy measurements

Spatial patterns of measured sub-canopy shortwave radiation were well replicated by the LiDAR synthetic images (Figure 6). The extent of solar transmission through the canopy at the two sites is well represented, both in location and magnitude. In general, the original LiDAR overestimated sub-canopy shortwave radiation compared to that measured (Table 2). Even very small sun-flecks at 1-2 m resolution, such as that in the southern-most corner of site 1 (Figure 6), were characterized by the model using the enhanced LiDAR.

RMSE values of modelled shortwave radiation using the enhanced LiDAR were significantly lower than that modelled using the original LiDAR (Table 2) and were within the range biases reported for similar model applications based on real HPs from Jonas et al. (2020). Mean bias and MAE values demonstrate the original LiDAR consistently overestimated sub-canopy shortwave radiation across both sites, while there was some underestimation with the enhanced LiDAR. Some disparities between measured and modelled radiation exist, particularly in the far eastern corner of site 1 (Figure 6), where a small amount of growth between LiDAR acquisition and radiation measurements has increased crown density to the south. Overall, however, patterns seen in the measured data were well replicated by the enhanced LiDAR and shortwave radiation model both in size, shape, positioning and magnitude of the radiation.

Site 2 can be characterized as diffuse radiation dominated during the measurement campaign, with only small sun-flecks in the south-western corner of the site. RMSE and positive mean biases of V_f and shortwave radiation at site 2 reveal an overestimation of shortwave radiation using the

original LiDAR compared to the enhanced. Gaps in the original LiDAR data resulted in an overestimation of V_f, which lead to an overestimation of diffuse radiation as well as an increase in the number of predicted sun-flecks throughout the site (Figure 6).

Errors presented in Table 2 demonstrate the importance of accurate and detailed canopy structure representation for estimating both diffuse and direct shortwave radiation. Accurate estimates of both direct and diffuse radiation are important within ecohydrological land surface models, for example, diffuse radiation has been shown to be important for photosynthesis (Law et al., 2002), while direct radiation has implications for canopy microclimate (Zellweger et al., 2019b) and local temperatures (Ehbrecht et al., 2019), influencing processes such as snowmelt (Musselman et al., 2012b). The performance of the shortwave radiation model using enhanced LiDAR to estimate both diffuse and direct radiation demonstrates how integrative approaches can simultaneously account for sun-flecks, canopy shading and local topographic effects to replicate measured sub-canopy radiation patterns. The combination of this integrative approach with spatially extensive LiDAR data can therefore assist in improving model estimates of sub-canopy shortwave radiation and associated ecohydrological processes across larger spatial scales at high spatial and temporal resolutions.

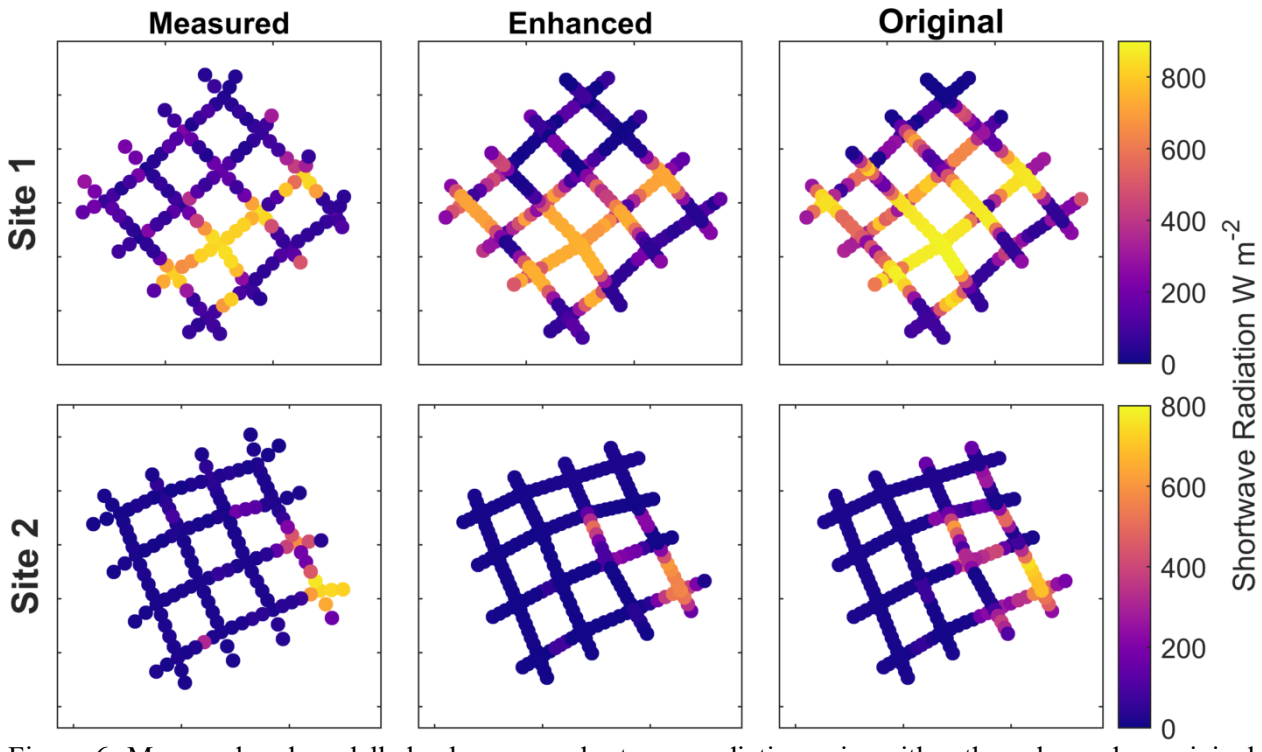

Figure 6: Measured and modelled sub-canopy shortwave radiation using either the enhanced or original LiDAR and measured above-canopy shortwave radiation at forest sites ("Gimbal" in Table 1). Modelled data is for the same measurement periods shown in Table 1. Spatial sampling intervals of measured and modelled data differs due to the movement of the sub-canopy radiometer during measurements. All images are oriented north to the top.

4.3.2 Comparison to aerial imagery

Spatially distributed modelling results using either the enhanced or the original LiDAR revealed detailed canopy shadows similar to those in the aerial imagery for the same time and location (Figure 7). Using both datasets, the height and structure of individual trees on the north-west side of the forest edge were well represented in the estimates of potential incoming shortwave radiation. Meter-scale differences between the two models are particularly noticeable within the forest, where there is a difference in the distribution and magnitude of sun-flecks between the two models (Figure 7d).

Further fine-scale discrepancies between the two model outputs are particularly noticeable in the differential map in Figure 7d, where, compared to the original LiDAR, the enhanced LiDAR lead to both higher (red) and lower (blue) estimates of total shortwave radiation. Most notable is the red outline of the canopy shadow boundary, where enhanced LiDAR estimates were greater than those from the original LiDAR. The need to increase projected point size distributions in the synthetic images of the original LiDAR lead to an increased canopy height and thickness, causing larger shadows compared to the enhanced LiDAR. The fact that these differences in canopy height were evident in the 1 m spatial resolution model demonstrates the method using the original LiDAR overestimates the shadow length at the time of the day by more than 1 m. Streaks of dark blue along the edges and within the canopy show where tree trunks and branches in the enhanced LiDAR have blocked canopy shortwave transmission compared to the original LiDAR (Figure 7d).

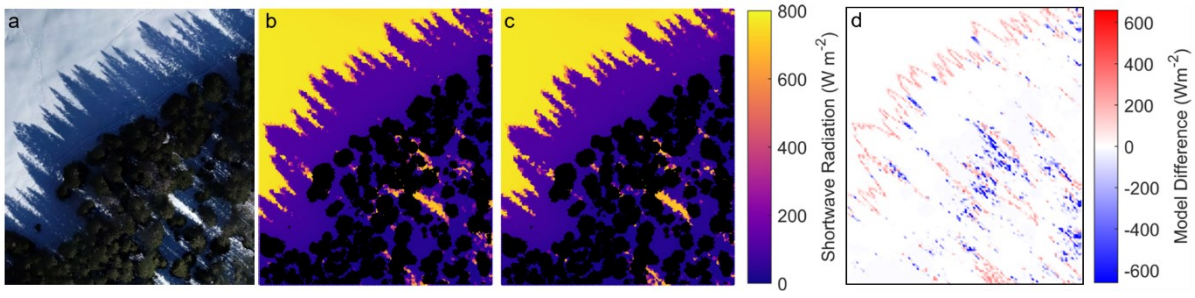

Figure 7: Imaged and modelled total shortwave radiation at 09:30am on 28.03.2019 along a northwest facing edge (110 m x 130 m domain) in the center of the flight area; a) aerial image; b) modelled using enhanced LiDAR; c) modelled using original LiDAR; d) difference between b and c (Original - Enhanced). All images are oriented north to the top. Area is shown in Figure 1c.

Repeat imaging flights over a larger 300 m x 360m area in the center of the model domain (Figure 1c) show the enhanced LiDAR and shortwave radiation model performed well over a range of

633 solar zenith and azimuth angles (Figure 8). Solar zenith angles were similar during flight 1 (Figure
634 8a and d) and flight 3 (Figure 8c and f) at 56° and 60°, respectively, but changes in solar azimuth
635 (128° to 236°) reveal differences in the size, shape and orientation of shadows across the flight
636 area. In explicitly accounting for canopy transmissivity in the path of the solar track, individual
637 sun-flecks and time dependent direct shortwave radiation were accurately modelled. For example,
638 a linear pathway running through the southern half of the flight area was only sun-lit under a
639 specific solar azimuth (flight 2 at 12:30; Figure 8b and e), which was accurately captured in the
640 model. These results highlight the importance of incorporating heterogeneous canopy structure
641 with both solar zenith and azimuth angles when modelling shortwave radiation.

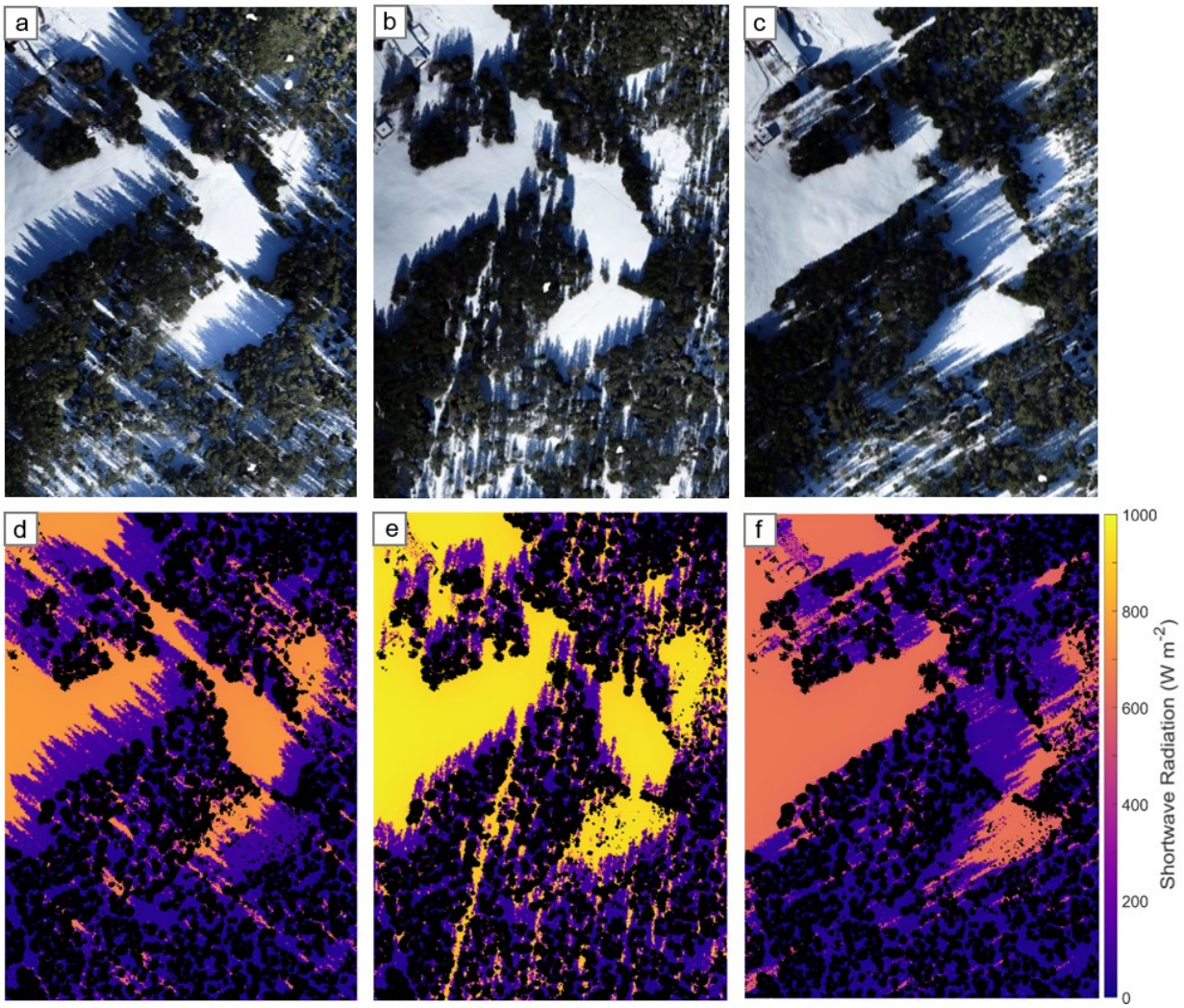

642

643 Figure 8: Comparison of imaged snow surface shadowing (a-c) and modelled shortwave radiation (d-f)
644 across the 300 m x 360m flight area (Figure 1c) at 09:30 (left; a,d), 12:30 (center; b,e) and 15:30 (right; c,f)
645 on 28.03.2019.

646

647 Discrepancies between modelled and imaged shadow patterns arise in the south of the flight area,
648 where selective logging in the nine years since data acquisition has led to a sparser canopy (Figure
649 8). These discrepancies between model and observations stress the importance of using up-to-date
650 datasets for modelling shortwave radiation. A suggested alternative to the expense of further

airborne LiDAR data collection would be to remove individual trees from the LiDAR dataset to represent the selective logging practices carried out since data acquisition. Over smaller modelling areas, such as the example used in this study, it would be possible that the LiDAR could be edited to remove specific trees that have been felled in reality. While this would require specific site knowledge, canopy segmentation algorithms would facilitate the identification and classification of individual trees and allow easy removal of the points from the LiDAR.

Further errors in the model occurred in close proximity to buildings, as seen in the north-western corner of the flight area (Figure 8). LiDAR data represent buildings as discrete points rather than opaque surfaces, which are not realistically represented in the synthetic hemispherical images. In future studies in areas where buildings are more predominant, buildings points could be enhanced with adequate density to ensure opaque surfaces.

An animation of the results across the full model domain for 28 March at 10-minute intervals as well as the winter and summer solstices is available in the supplementary material (Animation 2). Prior to the sun appearing above the local topography horizon, the detail of the spatial variability of diffuse light is apparent, particularly in the larger gaps in the south and center of the domain. The disappearance of shadows from west to east across the model domain during topographic sunrise further demonstrate the importance of the inclusion of topographic shading in mountainous regions. Rotation and increase/decrease in shadow size were fully resolved in both the spatial and temporal resolution of the model.

4.4 Calculation of gridded ground surface shading

From the estimated direct and diffuse solar radiation components, a binary mask can be calculated to determine whether the ground is shaded or not (Figure 9; Animation 3 in supplementary material). Here, a shaded point was defined as any area where the modelled diffuse component was larger than the modelled direct component. High resolution calculations of shaded ground surface across the entire model domain correspond well with modelled total radiation. Averaging these values at 25 m grid scales further result in a shading pattern that replicates that seen at higher resolution. For example, both resolutions show topography completely shades the north-west facing slopes in the south-east corner of the domain in the morning, while distribution and magnitude of gridded shading during the midday period match canopy densities across the domain (see Figure 1d for canopy height model).

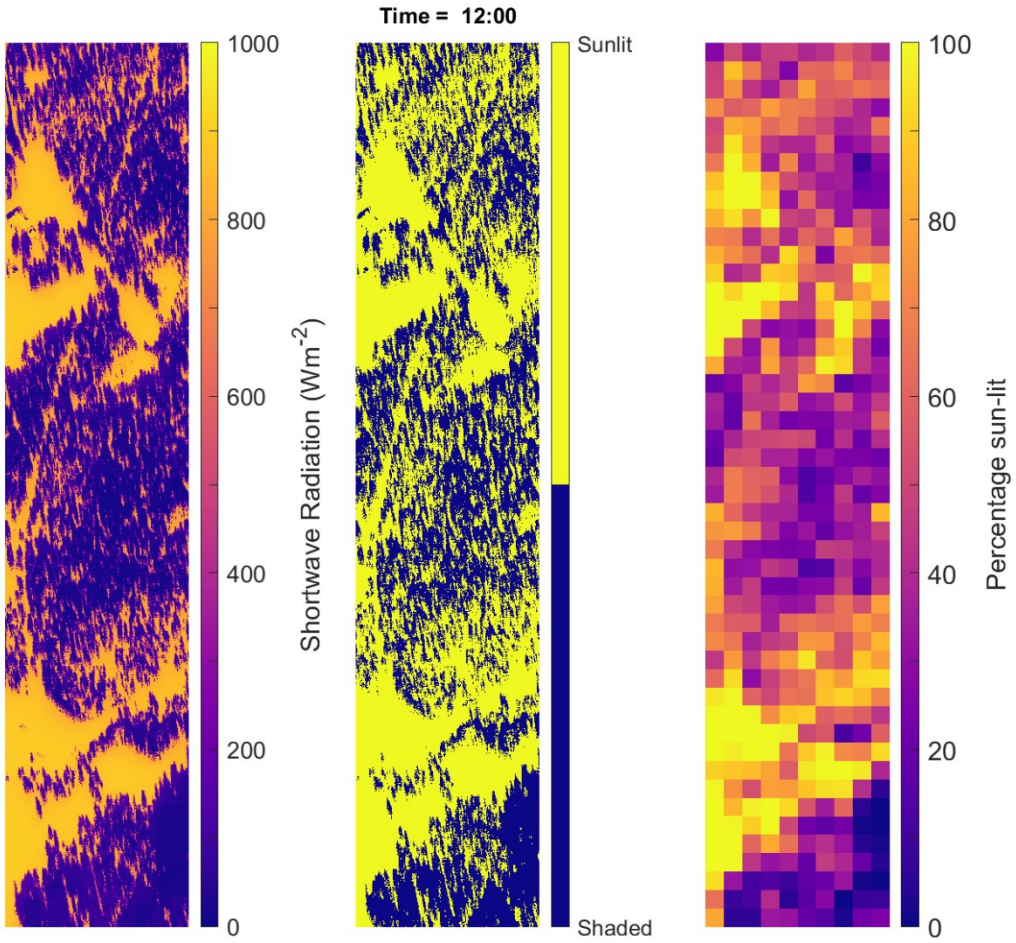

682

683 Figure 9: Midday snapshot of modelled incoming shortwave radiation at 1 m resolution (left); binary
684 shadows at 1 m resolution (center); 25 m x 25 m grid scale sun-lit fraction (right) for 28.03.2019 across
685 entire model domain. Model resolution was 1 m. Animation across the full daily solar cycle is available in
686 the supplementary material.

687

688 Snow surface shading has been demonstrated to be strongly correlated with, for example, up-
689 welling shortwave energy during snow cover (Malle et al. 2019; Webster and Jonas, 2018). In
690 particular, the calculated shaded-view fraction of the hemispherical view from a downward-

looking shortwave radiation sensor is strongly correlated with the measured up-welling global shortwave radiation (Malle et al. 2019). Improved representation of the sub-canopy shortwave radiation and associated shaded view fractions such as those shown in Figure 9 and Animation 3 could therefore contribute to estimation of the upwelling component of the shortwave energy budget at both high spatial and temporal resolution. This information would facilitate calculation of land surface albedo over landscape scales.

4.5 Implications for ecohydrological modelling

Differences in model errors between the original and enhanced LiDAR translate to different estimates of total daily solar radiation. Total daily radiation (maximum potential radiation) was modelled at the location shown in Figure 4c (X in Figure 10e), where the original LiDAR has a noticeably lower canopy density compared to the enhanced LiDAR (Figure 10b and c). From December to March, total daily radiation did not differ between the two models except for a slight overestimation by the original LiDAR, likely due to the overestimation of V_f and diffuse radiation. From March through to the June summer solstice, the original LiDAR consistently overestimated total daily incoming shortwave radiation (Figure 10d). These differences were particularly large during April and May, coinciding both with the snowmelt period and beginning of the growth season. During these periods, the original LiDAR estimated close to double the total daily radiation compared to the enhanced LiDAR. These significant improvements of the enhanced LiDAR compared to the original demonstrate how important accurate representation of the lower canopy within airborne LiDAR is for radiative transfer modelling.

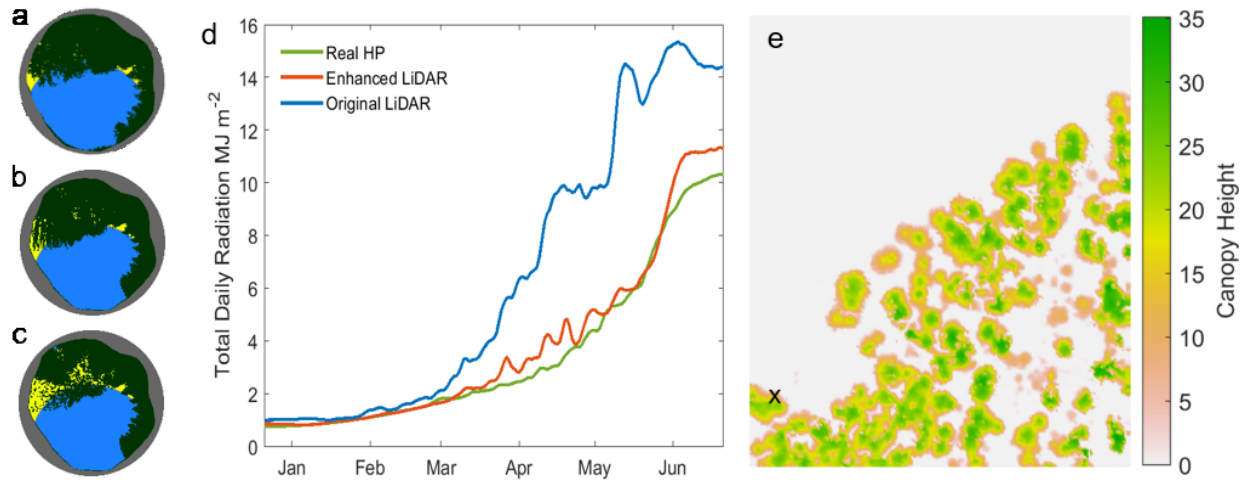

712

713 Figure 10: Changing solar position across a 6-month solar cycle shown in yellow within (a) the real
714 hemispherical photograph, (b) synthetic hemispherical images from the enhanced LiDAR and (c) original
715 LiDAR. Modelled total daily radiation across the same time period is shown in (d) and location is denoted
716 by X in the canopy height model in (e).

717

718 Differences between model output from the two LiDAR datasets observed at the point scale
719 translate to a strong association with canopy structure in spatially distributed simulations (Figure
720 11). Within denser canopy environments, the enhanced LiDAR reduced total daily shortwave
721 radiation compared to the original LiDAR throughout the annual solar cycle. The increase in
722 LiDAR point density reduces both the V_f and direct canopy transmissivity, seen already in the
723 model results at site 2 (Figure 6). Differences in estimated total daily radiation were largest in the
724 March and June comparisons, reflecting model results at the point scale in Figure 10. Within gaps,
725 the enhanced LiDAR increased total radiation compared to the original LiDAR (red in Figure 11),
726 likely owing to the reduced canopy height from the smaller projected point sizes in the synthetic
727 images. This effect was more pronounced during the lower solar angles in winter, while there was
728 less overall influence later in the season when the solar position was above the height of the canopy

729 for longer periods during the day. The opposite occurred within the canopy, where the blue regions
730 in Figure 11 show total daily radiation was reduced due to increased canopy density in the
731 enhanced LiDAR. These patterns reflect those seen at the point scale (Figure 10), as well as the
732 snapshot over the same area in Figure 7.

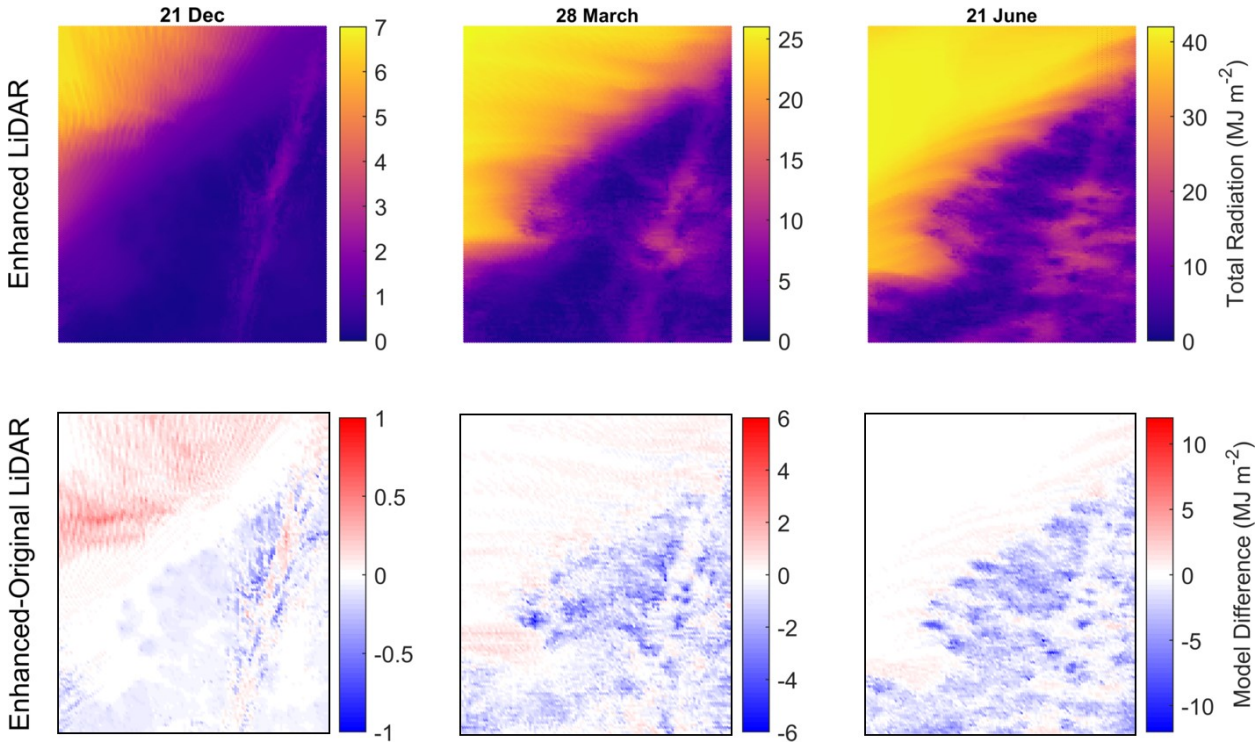

733

734 Figure 11: Top: Total potential daily radiation on 21 Dec, 28 March and 21 June estimated using the
735 enhanced LiDAR. Bottom: Difference in estimated total daily radiation from the enhanced and original
736 LiDAR. Blue colors denote where shortwave radiation was reduced by the LiDAR enhancement. Canopy
737 height model of area is shown in Figure 10e.

738

739 Improved estimates of canopy shortwave transmission through the LiDAR enhancement procedure
740 have crucial implications for the modelling of ecohydrological processes, particularly during the
741 snowmelt and subsequent growth season when model improvement was highest. Snowmelt models
742 using time-varying transmissivity from the enhanced LiDAR as input would predict slower melt

743 rates within forests and delayed snow disappearance dates compared to the original LiDAR, with
744 consequent effects on modelled streamflow timing and downstream hydrology. Improved
745 estimates of forest snow depletion would not only contribute to ecohydrological modelling, but
746 facilitate improved estimates of forest snow albedo within land surface schemes. Furthermore,
747 understanding of the sub-canopy light regime at high spatial and temporal resolution, coupled with
748 accurate estimates snow covered area would allow a more informed approach to estimate fractional
749 snow cover below the canopy.

750 During the growing season, estimates of sub-canopy shortwave radiation at high spatial and
751 temporal resolution using the enhanced LiDAR could aid model prediction of soil moisture content
752 and water availability following snowmelt. Estimates of modelled light availability for plants
753 would allow more detailed maps of species distributions, habitats and associated biodiversity.
754 Representation of fine-scale canopy shortwave transmissivity models through airborne LiDAR
755 enhancement procedures is therefore crucial for further understanding ecohydrological processes
756 in forest environments, but also biodiversity of plant and animal habitats and communities.

757

758 **4.6 Future directions**

759 The methodology presented in this study was developed for fairly high-resolution airborne LiDAR
760 data (> 20 points m^{-2}), previously used in forest radiative transfer modelling. Datasets of this
761 quality are commonly available for actively researched field areas. Lower resolution datasets (1-5
762 points m^{-2}) may produce less accurate estimates of locations of canopy maxima if LiDAR beams
763 have failed to hit the top of individual trees. The presented procedure to increase LiDAR point

764 density would likely not be applicable to these datasets without first accounting for underestimated
765 canopy heights and uncertainty in locations of canopy maxima. Musselman et al. (2013) found
766 good results by combining two lower resolution LiDAR datasets to obtain a higher resolution point
767 cloud, although care must be taken with ground returns when combining datasets from snow-on
768 and snow-off conditions (Ferraz et al., 2018). This solution would also only apply to evergreen
769 forests, or datasets acquired within the same season.

770 The addition of branch points in LiDAR data using the segmentation and classification method
771 should apply for most LiDAR datasets, irrespective of species, but the tree trunk delineation
772 procedure is currently limited to conifer species with vertical stem profiles, such as Pine, Fir or
773 Larch. Meanwhile, application of the shortwave model to datasets of deciduous species should be
774 treated with caution, and is likely limited to the time of year when the LiDAR dataset was
775 collected. Further model development using synthetic hemispherical images should address these
776 current limitations.

777

778 **5 CONCLUSIONS**

779 Through new canopy segmentation algorithms, a simple and efficient methodology was developed
780 for adding trunk and branch points to an existing airborne LiDAR dataset. The inclusion of these
781 points both increased the LiDAR point density across the model domain, and also improved the
782 representation of individual canopy elements, particularly in the lower canopy which is often
783 occluded from airborne data acquisition. The new enhanced LiDAR dataset significantly improved
784 resulting synthetic hemispherical images compared to those generated using the original LiDAR

785 dataset, yielding more realistic depictions of individual trees. Comparison with real hemispherical
786 photographs demonstrated substantial improvement in the representation of these canopy
787 structures in both dense and relatively sparse environments. Using the enhanced LiDAR,
788 distributions of sky-view fraction at each site were closer to measured distributions. Improved
789 synthetic hemispherical images were also ideally suited for accurately calculating time-varying
790 forest transmissivity for high spatiotemporal resolution modelling of diffuse and direct shortwave
791 radiation. During clear sky conditions, comparison of model output with both measured data and
792 aerial imagery of snow surface shading patterns further demonstrated the proficiency of the
793 enhanced LiDAR and the shortwave radiation model to resolve complex spatiotemporal patterns
794 in sun-fleck distributions.

795 These results comprise ideal data to validate and/or develop radiative transfer schemes of coarse
796 scale land-surface models even over larger areas. Because the model incorporates fine-scale
797 canopy discontinuities it can be used instead of bulk canopy descriptor parameters to improve
798 estimates of solar radiation input to sub-canopy environments, with benefits for snowmelt and
799 ecohydrological modelling at landscape scales. It can further provide maps of snow surface
800 shading at high spatiotemporal resolution for calculating effective surface albedo of forested areas
801 during wintertime, which have potential applications for forest snow reflectance observations and
802 land surface modelling.

803

6 ACKNOWLEDGEMENTS

Clare Webster and Giulia Mazzotti were supported by the Swiss National Science Foundation (P2SKP2_178173 and 200021_169213). The authors would like to thank Lucie Eberhard at SLF Davos for the aerial imagery in Figures 8 and 9, Magnus Hagdorn at the University of Edinburgh for computational support, Johanna Malle from Northumbria University for assistance with cable car operation, and two anonymous reviewers for their valuable comments on the manuscript. The LiDAR enhancement and synthetic hemispherical image calculations used in this study are available under https://github.com/c-webster/Lidar2HemiEval

7 REFERENCES

Alexander, C., Moeslund, J.E., Bøcher, P.K., Arge, L., Svenning, J.-C.C., 2013. Airborne laser scanner (LiDAR) proxies for understory light conditions. Remote Sens. Environ. 134, 152–161. https://doi.org/10.1016/j.rse.2013.02.028

Baldocchi, D.D., Law, B.E., Anthoni, P.M., 2000. On measuring and modeling energy fluxes above the floor of a homogeneous and heterogeneous conifer forest 102, 187–206.

Bales, R.C., Hopmans, J.W., O'Geen, A.T., Meadows, M., Hartsough, P.C., Kirchner, P., Hunsaker, C.T., Beaudette, D., 2011. Soil moisture response to snowmelt and rainfall in a Sierra Nevada mixed-conifer forest. Vadose Zo. J. 10, 786–799.

Barilotti, A., Turco, S., Alberti, G., 2006. LAI determination in forestry ecosystem by LiDAR data analysis, in: Proceedings of Workshop 3D Remote Sensing in Forestry, Vienna, Austria.

Bode, C.A., Limm, M.P., Power, M.E., Finlay, J.C., 2014. Subcanopy Solar Radiation model: Predicting solar radiation across a heavily vegetated landscape using LiDAR and GIS solar radiation models. Remote Sens. Environ. 154, 387–397. https://doi.org/10.1016/j.rse.2014.01.028

Breshears, D.D., Rich, P.M., Barnes, F.J., Campbell, K., 1997. Overstory-imposed heterogeneity in solar radiation and soil moisture in a semiarid woodland. Ecol. Appl. 7, 1201–1215.

Colin, F., Houllier, F., 1992. Branchiness of Norway spruce in northeastern France: predicting the main crown characteristics from usual tree measurements. Ann. For. Sci. 49, 511–538.

831 Dalponte, M., 2016. R Package'itcSegment': User Manual.

832 Dalponte, M., Coomes, D.A., 2016. Tree-centric mapping of forest carbon density from airborne laser
833 scanning and hyperspectral data. Methods Ecol. Evol. 7, 1236–1245. https://doi.org/10.1111/2041-
834 210X.12575

835 Ehbrecht, M., Schall, P., Ammer, C., Fischer, M., Seidel, D., 2019. Effects of structural heterogeneity on
836 the diurnal temperature range in temperate forest ecosystems. For. Ecol. Manage. 432, 860–867.

837 Erbs, D.G., Klein, S.A., Duffle, J.A., 1982. Estimation of the diffuse radiation fraction for hourly, daily and
838 monthly-average global radiation. Solar Energy 28 (4), 10.

839 Essery, R., Bunting, P., Rowlands, A., Rutter, N., Hardy, J., Melloh, R., Link, T., Marks, D., Pomeroy, J.,
840 2008. Radiative Transfer Modeling of a Coniferous Canopy Characterized by Airborne Remote
841 Sensing. J. Hydrometeorol. 9, 228–241. https://doi.org/10.1175/2007JHM870.1

842 Ferraz, A., Saatchi, S., Bormann, K.J. and Painter, T.H., 2018. Fusion of NASA Airborne Snow
843 Observatory (ASO) lidar time series over mountain forest landscapes. Remote Sensing, 10(2), p.164.

844 Frazer, G.W., Canham, C.D., Lertzman, K.P., 1999. Gap Light Analyzer (GLA), Version 2.0: Imaging
845 software to extract canopy structure and gap light transmission indices from true-colour fisheye
846 photographs, users manual and program documentation. Simon Fraser Univ. Burn. Br. Columbia, Inst.
847 Ecosyst. Stud. Millbrook, New York 36.

848 Gray, H.R., 1956. The form and taper of forest-tree stems. Imperial Forestry Institute, University of Oxford
849 UK.

850 Haddad, N.M., Brudvig, L.A., Clobert, J., Davies, K.F., Gonzalez, A., Holt, R.D., Lovejoy, T.E., Sexton,
851 J.O., Austin, M.P., Collins, C.D., Cook, W.M., Damschen, E.I., Ewers, R.M., Foster, B.L., Jenkins,
852 C.N., King, A.J., Laurance, W.F., Levey, D.J., Margules, C.R., Melbourne, B.A., Nicholls, A.O.,
853 Orrock, J.L., Song, D., Townshend, J.R., 2015. Habitat fragmentation and its lasting impact on Earth
854 ' s ecosystems. Appl. Ecol. 1–9. https://doi.org/10.1126/sciadv.1500052

855 Hamraz, H., Contreras, M.A., Zhang, J., 2017. Vertical stratification of forest canopy for segmentation of
856 understory trees within small-footprint airborne LiDAR point clouds. ISPRS J. Photogramm. Remote
857 Sens. 130, 385–392.

858 Hancock, S., Essery, R., Reid, T., Carle, J., Baxter, R., Rutter, N., Huntley, B., 2014. Characterising forest
859 gap fraction with terrestrial lidar and photography: An examination of relative limitations. Agric. For.
860 Meteorol. 189–190, 105–114. https://doi.org/10.1016/j.agrformet.2014.01.012

861 Hardy, J.P., Melloh, R., Koenig, G., Marks, D., Winstral, A., Pomeroy, J.W., Link, T., 2004. Solar radiation
862 transmission through conifer canopies. Agric. For. Meteorol. 126, 257–270.
863 https://doi.org/10.1016/j.agrformet.2004.06.012

864 Harpold, A.A., Guo, Q., Molotch, N., Brooks, P.D., Bales, R., Fernandez-Diaz, J.C., Musselman, K.N.,
865 Swetnam, T.L., Kirchner, P., Meadows, M.W., Flanagan, J., Lucas, R., 2014. LiDAR-derived
866 snowpack data sets from mixed conifer forests accross the Western United States. Water Resour. Res.
867 50, 2749–2755. https://doi.org/10.1002/2013WR013935.Received

868 Jonas, T., Webster, C., Mazzotti, G., Malle, J., 2020. HPEval: A canopy shortwave radiation transmission
869 model using high-resolution hemispherical images. Agric. For. Meteorol. 284, 107903.
870 https://doi.org/https://doi.org/10.1016/j.agrformet.2020.107903

871 Jucker, T., Caspersen, J., Chave, J., Antin, C., Barbier, N., Bongers, F., Dalponte, M., van Ewijk, K.Y.,
872 Forrester, D.I., Haeni, M., 2017. Allometric equations for integrating remote sensing imagery into
873 forest monitoring programmes. Glob. Chang. Biol. 23, 177–190.

874 Kane, V. R., Gillespie, A. R., McGaughey, R., Lutz, J. A., Ceder, K., & Franklin, J. F. (2008). Interpretation
875 and topographic compensation of conifer canopy self-shadowing. Remote sensing of
876 Environment, 112(10), 3820-3832.

877 Khosravipour, A., Skidmore, A.K., Isenburg, M., Wang, T., Hussin, Y.A., 2014. Generating Pit-free
878 Canopy Height Models from Airborne Lidar. Photogramm. Eng. Remote Sens. 80, 863–872.
879 https://doi.org/10.14358/PERS.80.9.863

880 King, J.Y., Brandt, L.A., Adair, E.C., 2012. Shedding light on plant litter decomposition: advances,
881 implications and new directions in understanding the role of photodegradation. Biogeochemistry 111,
882 57–81. https://doi.org/10.1007/s10533-012-9737-9

883 Law, B.E., Falge, E., Gu, L. v, Baldocchi, D.D., Bakwin, P., Berbigier, P., Davis, K., Dolman, A.J., Falk,
884 M., Fuentes, J.D., 2002. Environmental controls over carbon dioxide and water vapor exchange of
885 terrestrial vegetation. Agric. For. Meteorol. 113, 97–120.

886 Lawler, R.R., Link, T.E., 2011. Quantification of incoming all-wave radiation in discontinuous forest
887 canopies with application to snowmelt prediction. Hydrol. Process. 25, 3322–3331.
888 https://doi.org/10.1002/hyp.8150

889 Leuschner, C., Rode, M.W., 1999. The role of plant resources in forest succession: changes in radiation,
890 water and nutrient fluxes, and plant productivity over a 300-yr-long chronosequence in NW-Germany.
891 Perspect. Plant Ecol. Evol. Syst. 2, 103–147.

892 Link, T.E., Marks, D., 1999. Point simulation of seasonal snow cover dynamics beneath boreal forest
893 canopies. J. Geophys. Res. 104, 27841. https://doi.org/10.1029/1998JD200121

894 Mäkinen, H., Hein, S., 2006. Effect of wide spacing on increment and branch properties of young Norway
895 spruce. Eur. J. For. Res. 125, 239–248.

896 Malle, J., Rutter, N., Mazzotti, G., Jonas, T., 2019. Shading by trees and fractional snow cover control the
897 subcanopy radiation budget. J. Geophys. Res. Atmos. 124, 3195–3207.

898 Mazzotti, G., Malle, J., Barr, S., Jonas, T., 2019. Spatially continuous characterization of forest canopy
899 structure and sub-canopy irradiance derived from handheld radiometer surveys. J. Hydrometeorol.

900 Moeser, D., Roubinek, J., Schleppi, P., Morsdorf, F., Jonas, T., 2014. Canopy closure, LAI and radiation
901 transfer from airborne LiDAR synthetic images. Agric. For. Meteorol. 197, 158–168.
902 https://doi.org/10.1016/j.agrformet.2014.06.008

903 Morsdorf, F., Kötz, B., Meier, E., Itten, K.I., Allgöwer, B., 2006. Estimation of LAI and fractional cover
904 from small footprint airborne laser scanning data based on gap fraction. Remote Sens. Environ. 104,

50–61. https://doi.org/10.1016/j.rse.2006.04.019

Musselman, K.N., Margulis, S.A., Molotch, N.P., 2013. Estimation of solar direct beam transmittance of conifer canopies from airborne LiDAR. Remote Sens. Environ. 136, 402–415. https://doi.org/10.1016/j.rse.2013.05.021

Musselman, K.N., Molotch, N.P., Margulis, S.A., Kirchner, P.B., Bales, R.C., 2012a. Influence of canopy structure and direct beam solar irradiance on snowmelt rates in a mixed conifer forest. Agric. For. Meteorol. 161, 46–56. https://doi.org/10.1016/j.agrformet.2012.03.011

Musselman, K.N., Molotch, N.P., Margulis, S.A., Lehning, M., Gustafsson, D., 2012b. Improved snowmelt simulations with a canopy model forced with photo-derived direct beam canopy transmissivity. Water Resour. Res. 48, 1–21. https://doi.org/10.1029/2012WR012285

Ni, W., Woodcock, C.E., 2000. Effect of canopy structure and the presence of snow on the albedo of boreal conifer forests. J. Geophys. Res. Atmos. 105, 11879–11888. https://doi.org/10.1029/1999JD901158

Nijssen, B., Lettenmaier, D.P., 1999. A simplified approach for predicting shortwave radiation transfer through boreal forest canopies. J. Geophys. Res. Atmos. 104, 27859–27868.

Nolin, A.W., 2004. Towards retrieval of forest cover density over snow from the Multi-angle Imaging SpectroRadiometer (MISR). Hydrol. Process. 18, 3623–3636. https://doi.org/10.1002/hyp.5803

Nyman, P., Metzen, D., Hawthorne, S.N.D., Duff, T.J., Inbar, A., Lane, P.N.J., Sheridan, G.J., 2017. Evaluating models of shortwave radiation below Eucalyptus canopies in SE Australia. Agric. For. Meteorol. 246, 51–63. https://doi.org/10.1016/j.agrformet.2017.05.025

Plowright, A., 2018. Canopy analysis in r using ForestTools.

Raleigh, M.S., Rittger, K., Moore, C.E., Henn, B., Lutz, J.A. and Lundquist, J.D., 2013. Ground-based testing of MODIS fractional snow cover in subalpine meadows and forests of the Sierra Nevada. Remote Sensing of Environment, 128, pp.44-57.

Reid, T.D., Essery, R.L.H., Rutter, N., King, M., 2014. Data-driven modelling of shortwave radiation transfer to snow through boreal birch and conifer canopies. Hydrol. Process. 28, 2987–3007. https://doi.org/10.1002/hyp.9849

Schleppi, P., Conedera, M., Sedivy, I., Thimonier, A., 2007. Correcting non-linearity and slope effects in the estimation of the leaf area index of forests from hemispherical photographs. Agric. For. Meteorol. 144, 236–242.

Silva, C.A., Crookston, N.L., Hudak, A.T., Vierling, L.A., Klauberg, C., Silva, M.C.A., 2017. Package 'rLiDAR.'

Tymen, B., Vincent, G., Courtois, E.A., Heurtebize, J., Dauzat, J., Marechaux, I., Chave, J., 2017. Quantifying micro-environmental variation in tropical rainforest understory at landscape scale by combining airborne LiDAR scanning and a sensor network. Ann. For. Sci. 74, 32.

Varhola, A., Frazer, G.W., Teti, P., Coops, N.C., 2012. Estimation of forest structure metrics relevant to hydrologic modelling using coordinate transformation of airborne laser scanning data. Hydrol. Earth

941 Syst. Sci. 16, 3749–3766. https://doi.org/10.5194/hess-16-3749-2012

942 Vikhamar, D., Solberg, R., 2002. Subpixel mapping of snow cover in forests by optical remote sensing.
943 Remote Sens. Environ. 84, 69–82. https://doi.org/10.1016/S0034-4257(02)00098-6

944 Wan, Z., Dozier, J., Member, A., 1996. A Generalized Split- Window Algorithm for Retrieving Land-
945 Surface Temperature from Space 34, 892–905.

946 Webster, C., Jonas, T., 2018. Influence of canopy shading and snow coverage on effective albedo in a snow-
947 dominated evergreen needleleaf forest. Remote Sens. Environ. 214.
948 https://doi.org/10.1016/j.rse.2018.05.023

949 Widlowski, J.-L., Mio, C., Disney, M., Adams, J., Andredakis, I., Atzberger, C., Brennan, J., Busetto, L.,
950 Chelle, M., Ceccherini, G., 2015. The fourth phase of the radiative transfer model intercomparison
951 (RAMI) exercise: Actual canopy scenarios and conformity testing. Remote Sens. Environ. 169, 418–
952 437.

953 Zellweger, F., Baltensweiler, A., Schleppi, P., Huber, M., Küchler, M., Ginzler, C., Jonas, T., 2019a.
954 Estimating below-canopy light regimes using airborne laser scanning: An application to plant
955 community analysis. Ecol. Evol. 9, 9149–9159.

956 Zellweger, F., De Frenne, P., Lenoir, J., Rocchini, D., Coomes, D., 2019b. Advances in microclimate
957 ecology arising from remote sensing. Trends Ecol. Evol.

958

959

LIST OF FIGURE AND TABLE CAPTIONS

Figure 1: a) Location of study area within Eastern Swiss Alps and b) surrounding local topography; c) Solid red box outlines larger modelling domain, orange dashed line indicates flight area for aerial photography, dashed red box outlines smaller modelling domain shown in Figures 7 and 11, numbers show radiation measurement grid locations and 'o' shows location of open site; green circle indicates cable car location; green dashed line indicates transect location in Animation 1 in the supplementary material; d) canopy height model of modelling domain with boxed outlines of sites 1 and 2 and cable car location (lines); e) surface terrain height of modelling domain. Aerial imagery downloaded from https://s.geo.admin.ch/842c6f920c. Elevation data in a-b from https://shop.swisstopo.admin.ch/en/products/height_models/dhm25.

Figure 2: Canopy height model at 0.5 m resolution (a), with location of canopy maxima (b) and individual canopy segments (c) for an example 200 m x 200 m area in center of the model domain.

Figure 3: 15 m wide forest cross section along cable car transect (Figure 1c-d) with original LiDAR (top) and enhanced LiDAR (bottom).

Figure 4: Real hemispherical photographs (a-c), synthetic hemispherical images from enhanced LiDAR (d-f) and from original LiDAR (g-i) at three sample locations within Figure 2. South at top of picture. Real hemispherical photographs in a-c are radially distorted due to the non-linear projection of the lens (distortion was accounted for in all calculations).

Figure 5: Canopy height model and estimated V_f from real hemispherical photographs and synthetic hemispherical images from enhanced and original LiDAR at both forest sites. All images are oriented north to the top.

Figure 6: Measured and modelled sub-canopy shortwave radiation using either the enhanced or original LiDAR and measured above-canopy shortwave radiation at forest sites ("Gimbal" in Table 1). Modelled data is for the same measurement periods shown in Table 1. Spatial sampling intervals of measured and modelled data differs due to the movement of the sub-canopy radiometer during measurements. All images are oriented north to the top.

Figure 7: Imaged and modelled total shortwave radiation at 09:30am on 28.03.2019 along a northwest facing edge (110 m x 130 m domain) in the center of the flight area; a) aerial image; b) modelled using enhanced LiDAR; c) modelled using original LiDAR; d) difference between b and c (Original - Enhanced). All images are oriented north to the top. Area is shown in Figure 1c.

Figure 8: Comparison of imaged snow surface shadowing (a-c) and modelled shortwave radiation (d-f) across the 300 m x 360m flight area (Figure 1c) at 09:30 (left; a,d), 12:30 (center; b,e) and 15:30 (right; c,f) on 28.03.2019.

Figure 9: Midday snapshot of modelled incoming shortwave radiation at 1 m resolution (left); binary shadows at 1 m resolution (center); 25 m x 25 m grid scale sun-lit fraction (right) for 28.03.2019 across entire model domain. Model resolution was 1 m. Animation across the full daily solar cycle is available in the supplementary material.

Figure 10: Changing solar position across a 6-month solar cycle shown in yellow within (a) the real hemispherical photograph, (b) synthetic hemispherical images from the enhanced LiDAR and (c) original

998 LiDAR. Modelled total daily radiation across the same time period is shown in (d) and location is denoted
999 by X in the canopy height model in (e).

1000 Figure 11: Top: Total potential daily radiation on 21 Dec, 28 March and 21 June estimated using the
1001 enhanced LiDAR. Bottom: Difference in estimated total daily radiation from the enhanced and original
1002 LiDAR. Blue colors denote where shortwave radiation was reduced by the LiDAR enhancement. Canopy
1003 height model of area is shown in Figure 10e.

1004

1005 Table 1: Summary of canopy structure and data acquisition times for forest and open sites. Details of
1006 acquisition of hemispherical photographs (HPs) are classified as either validation (v) or calibration (c)
1007 measurements. Measurements were taken from a cable car (c.f. 2.3) and using a motorized gimbal set up
1008 (c.f. 2.4) and at an open site.

1009 Table 2: Root mean square error (RMSE), mean bias and mean absolute error (MAE) for sky-view fraction
1010 (V_f, dimensionless) and measured shortwave radiation (W m^{-2}) at the two forest sites.

1011